



# Evaluation of breaking wave effects in liquid sloshing problems: ANCF/SPH comparative study

Mohammed M. Atif · Sheng-Wei Chi · Emanuele Grossi · Ahmed A. Shabana

Received: 8 November 2018 / Accepted: 29 March 2019 / Published online: 4 May 2019  
© Springer Nature B.V. 2019

**Abstract** This paper is focused on evaluating the effect of breaking waves in liquid sloshing problems. Two fundamentally different approaches, namely the *smoothed particle hydrodynamics* (SPH) and the finite element (FE) *absolute nodal coordinate formulation* (ANCF), are used to describe the liquid sloshing response in several sloshing scenarios. The SPH method is a mesh-free numerical technique often used to capture very large displacements in fluid and solid mechanics problems. ANCF finite elements, on the other hand, can be used to develop a non-incremental solution procedure, suited for the nonlinear analysis of flexible bodies undergoing large rotation and large deformation. The fundamental differences between the two approaches and the advantages and limitations of each are discussed. Two benchmark problems, the *dam break* and *sloshing tank*, are used to perform a detailed SPH/ANCF quantitative comparative study in different sloshing scenarios. While a good agreement is found

between the ANCF and SPH converged solutions for the dam break problem, in the sloshing tank problem the SPH solution underpredicts the amplitude of oscillation of the fluid center of mass and the wave height at a selected probe point. Because one ANCF element can capture complex shapes, nearly 40 times fewer degrees of freedom than the SPH model are needed in both problems. The use of the ANCF models leads to a CPU saving of 70% and 25% in the broken dam and sloshing tank problems, respectively. In the case of the tank problem, the effect of light, moderate, and severe turbulence is examined. The position of the fluid center of mass is computed using the two approaches, and the results obtained are verified using a reference analytical solution. The power spectral density of the center of mass is evaluated using the fast Fourier transform (FFT) to study the effect of breaking waves. The results show that in the case of light and moderate turbulence, the ANCF model allows for accurately averaging the fluid inertia properties, and the obtained solutions are in good agreement with the SPH solutions. In the case of severe turbulence, on the other hand, the mechanical energy dissipation due to fluid mixing and wave breaking, which can only be captured using the SPH method, damps out the sloshing oscillations.

---

M. M. Atif · S.-W. Chi  
Department of Civil and Material Engineering, University of Illinois at Chicago, Chicago, IL 60607, USA  
e-mail: matif2@uic.edu

S.-W. Chi  
e-mail: swchi@uic.edu

E. Grossi · A. A. Shabana (✉)  
Department of Mechanical and Industrial Engineering, University of Illinois at Chicago, Chicago, IL 60607, USA  
e-mail: shabana@uic.edu

E. Grossi  
e-mail: egross20@uic.edu

**Keywords** Turbulence · Breaking waves · Liquid sloshing · Absolute nodal coordinate formulation · Smoothed particle hydrodynamics · Dam break

## 1 Introduction

Liquid sloshing phenomena play an important role in automotive, civil, marine, and aerospace engineering. Several analytical and numerical methods have been developed in the literature to study the static and dynamic properties of fluids moving in partially filled containers. The development of analytical methods for the analysis of liquid sloshing is very challenging because dynamic boundary conditions at the free surface are nonlinear and the position time history of the liquid free surface is not known a priori. For these reasons, the analytical methods developed in the literature are more suited to simplified scenarios characterized by regular geometric tank shapes and a small-amplitude sloshing motion [34,35].

Most of the numerical methods developed to solve liquid sloshing problems are based on two different approaches, namely *Lagrangian* and *Eulerian*. In the former approach, the mesh is attached to the fluid material points, while in the latter approach the domain under investigation is discretized using a stationary mesh. Eulerian techniques are particularly suited for the study of turbulent flow, but the identification of the fluid free surface is not straightforward and requires using a very refined mesh. On the other hand, Lagrangian methods are accurate in predicting the location of the fluid free surface, but the loss in numerical accuracy resulting from severe deformations requires the use of adaptive remeshing algorithms. In order to address the difficulties encountered by grid-based numerical methods in the study of physical systems which exhibit very large deformations, such as liquid sloshing, several mesh-free methods have been developed [42].

Among the most popular mesh-free methods, the *smoothed particle hydrodynamic* (SPH) has been widely used in the field of fluid dynamics to study complex systems characterized by turbulence and multiphase flow. The level of difficulty in the analysis of liquid sloshing problems increases considerably when the container is component of a complex mechanical system such as a tanker truck, a railroad vehicle, or a spacecraft. A recently proposed total Lagrangian continuum-based liquid sloshing approach based on the *absolute nodal coordinate formulation* (ANCF) allows for a systematic integration of fluid and vehicle models using multibody system (MBS) algorithms [78].

In the field of ocean and coastal engineering, hydrodynamic impact loads due to liquid sloshing can have

an effect on the structural integrity of marine systems. The study of breaking waves has been the subject of several investigations in the field of liquefied natural gas (LNG) vessels and Naval engineering [8,10–12,16,23,33,61,64]. In the field of vehicle system dynamics, on the other hand, the main concern is not the effect of liquid sloshing on the structural integrity of the containers, but rather on the vehicle dynamics and stability. In order to analyze the effect of liquid sloshing on the vehicle dynamics and stability, the average liquid motion inside the container and the time-varying fluid inertia forces are the main focus. For this reason, simple approaches based on models with rigid bodies representing the fluid motion are often used when the vehicle or container dynamics and stability are the main concern. Continuum-based ANCF sloshing formulations have been recently proposed for the implementation in MBS algorithms to study the effect of liquid sloshing on vehicle dynamics. In sloshing scenarios, however, turbulence may occur, and therefore, it is necessary to quantify and evaluate its effect on the average nominal motion of the fluid. Several researchers investigated the breaking wave effects induced by nonlinear sloshing motion using the finite element and finite difference methods [15,31,39–41,44,46,47,74]. In this paper, the effect of breaking waves on the average nominal motion of the fluid is examined by developing two different models; a continuum-based ANCF model that can accurately represent the nominal motion, but does not capture the effect of turbulence; and a mesh-free SPH model that can capture the turbulence effect. Comparison between the results of these two models will shed light on the significance of the turbulence effect in sloshing scenarios. It will also shed light on the model accuracies as well as the computational cost.

The main goal of this paper is to perform for the first time a detailed comparative quantitative study of the effect of turbulence and wave breaking phenomena on liquid sloshing using the SPH and ANCF methods. This paper makes the following specific contributions:

- (1) The paper describes the ANCF and SPH discretization to obtain the discrete dynamic equations which govern liquid sloshing phenomena. Based on this description, the fundamental differences between the ANCF and SPH approaches are discussed.
- (2) A detailed quantitative comparison between the ANCF and SPH approaches when solving sloshing

problems is performed. The comparative numerical study is focused on evaluating both the accuracy and computational cost of the two different approaches. To this end, two benchmark examples are used; the dam break and sloshing tank benchmark problems. These two benchmark problems are solved for different motion scenarios in order to compare the results of different ANCF and SPH models.

- (3) The effects of breaking waves on liquid sloshing dynamics are investigated. The good agreement between the ANCF and SPH results in the case of light and moderate turbulence scenarios demonstrates that ANCF finite elements can accurately predict the nominal fluid motion and inertia forces. In case of severe turbulence, it is found that the ANCF approach overpredicts the amplitude of oscillations of the fluid center of mass as compared to the SPH method, due to the absence of mechanical energy dissipation associated with the fluid mixing.
- (4) The ANCF liquid sloshing results are validated against experimental data, and verified using the results of the SPH models. The validation and verification of the ANCF liquid sloshing approach are necessary in order to justify using such a new approach in future liquid sloshing investigations, particularly when complex motion scenarios are considered.

The paper is organized as follows. In Sect. 2, the basic governing equations of the liquid sloshing phenomena are presented, while the solution procedures used in this investigation for solving these equations using the SPH and ANCF approaches are presented in Sects. 3 and 4, respectively. Section 5 provides a summary of the fundamental differences between the SPH and ANCF approaches. In Sect. 6, the numerical results obtained for the two benchmark problems are validated against experimental data, and the effects of breaking waves on liquid sloshing dynamics are discussed. Section 7 presents a summary and the main conclusions drawn from this study.

## 2 Basic governing equations

The dynamic behavior of fluids is governed by the Navier–Stokes equations, derived by combining the

continuity and momentum balance equations. The continuity equation is written as

$$\frac{\partial \rho}{\partial t} + \nabla \cdot (\rho \mathbf{v}) = 0 \tag{1}$$

where  $\rho$  is the mass density,  $t$  is time, and  $\mathbf{v}$  is the velocity vector. In the case of incompressible materials, Eq. 1 reduces to  $\nabla \cdot \mathbf{v} = 0$ . The momentum balance equation can be written as

$$\rho \mathbf{a} = \nabla \cdot \boldsymbol{\sigma} + \mathbf{b} \tag{2}$$

where  $\mathbf{a} = d\mathbf{v}/dt$  is the absolute acceleration vector,  $\mathbf{b}$  is the body force vector, and  $\boldsymbol{\sigma}$  is the Cauchy stress tensor. In the case of isotropic Newtonian fluids, the fluid constitutive equations can be written as

$$\boldsymbol{\sigma} = -[p + \lambda \text{tr}(\mathbf{D})] \mathbf{I} + 2\mu \mathbf{D} \tag{3}$$

where  $p$  is the hydrostatic pressure,  $\mathbf{D} = (\nabla \mathbf{v} + (\nabla \mathbf{v})^T)/2$  is the rate of deformation tensor,  $\nabla \mathbf{v}$  is the gradient of the velocity vector,  $\text{tr}$  is the trace operator,  $\mathbf{I}$  is the  $3 \times 3$  identity matrix, and  $\lambda$  and  $\mu$  are viscosity coefficients. Substituting the expression of the stress defined in Eq. 3 into Eq. 2, one obtains the Navier–Stokes equations

$$\rho \mathbf{a} = -\nabla \cdot (p \mathbf{I}) + \lambda \nabla \cdot (\text{tr}(\mathbf{D}) \mathbf{I}) + 2\mu \nabla \cdot \mathbf{D} + \mathbf{b} \tag{4}$$

In the case of incompressible fluids, Eq. 4 reduces to

$$\mathbf{a} = -\frac{\nabla p}{\rho} + \frac{\mu}{\rho} \nabla^2 \mathbf{v} + \frac{\mathbf{b}}{\rho} \tag{5}$$

where  $\nabla^2$  is the Laplace operator. In the following sections, the ANCF and SPH formulations and procedures used to obtain the solution of Eq. 4 are discussed. This discussion will shed light on the fundamental differences between the two approaches.

## 3 SPH approach

The *smoothed particle hydrodynamics* (SPH) method is a mesh-free, particle-based, Lagrangian numerical technique first introduced by Lucy [53] and Gingold and Monaghan [22]. The SPH method was successfully applied to complex problems, such as fracture, blast, penetration, impact and fluid free surface [6, 7, 9, 24, 25,

38,42,43,45,48,65,76]. The analysis of liquid sloshing problems using the SPH method has been studied by modifying the spatial derivative and by accounting for the boundary particles [17,70]. Several investigations on multiphase flow and surface tension problems have been performed using the SPH method [26,32,58,60].

While the SPH method has several advantages, it also has its own technical drawbacks. Wen et al. [79] developed the conservative smoothing approach as a cure for tensile instability. The SPH method also has difficulty in enforcing boundary conditions, which was later rectified by Randles and Libersky [66]. The stability and convergence analysis of mesh-free methods have been studied by Belytschko et al. [3–5]. The first SPH penalty contact algorithm was developed by Vignjevic and Campbell [75]. However, it was shown that this approach often excited zero energy modes. Beissel and Belytschko [2] proposed an alternative method to stabilize nodal integration, referred to as the least square stabilization method. Chen et al. [14] and Chen and Beraun [13] proposed a *corrective smoothed particle method* (CSPM) to improve the calculation accuracy.

The SPH method can be developed using the kernel estimate. A function  $A(\mathbf{x})$  can be approximated by smoothing kernel functions  $\phi_h(\mathbf{x} - \mathbf{x}_j)$  centered around  $\mathbf{x}$  as

$$A(\mathbf{x}) \approx \sum_{j=1}^N \phi_h(\mathbf{x} - \mathbf{x}_j) A(\mathbf{x}_j) \Delta V_j, \forall \mathbf{x}_j \in \Omega_s \tag{6}$$

where  $\Omega_s$  is the domain,  $\Delta V_j = m_j/\rho_j$ ,  $m_j$ ,  $\rho_j$ , and  $\mathbf{x}_j$  are the nodal volume, mass, mass density, and position of particle  $j$ , respectively, and  $N$  is the total number of particles within the support domain of the smoothing function at  $\mathbf{x}$ . If the kernel selected is sufficiently smooth, the gradient of the approximation function  $A(\mathbf{x})$  is calculated as

$$\nabla A(\mathbf{x}) \approx \sum_{j=1}^N \nabla \phi_h(\mathbf{x} - \mathbf{x}_j) A(\mathbf{x}_j) \Delta V_j \tag{7}$$

Several smoothing kernel functions can be used, such as the cubic spline function defined as

$$\phi_h(q) = \frac{C}{h^n} \begin{cases} 1 - \frac{3}{2}q^2 + \frac{3}{4}q^3 & 0 \leq q \leq 1 \\ \frac{1}{4}(2 - q)^3 & 1 \leq q \leq 2 \\ 0 & \text{otherwise} \end{cases} \tag{8}$$

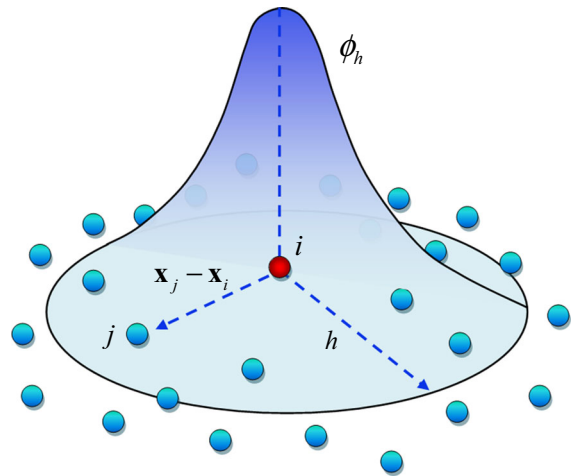


**Fig. 1** Schematic illustration of a SPH smoothing kernel function in the three-dimensional case

where  $h$  is the smoothing length or support size,  $q = \|\mathbf{x} - \mathbf{x}_j\|/h$ ,  $n$  is the space dimension, and  $C$  is a normalization factor, defined as

$$C = \begin{cases} 2/3 & n = 1 \\ 10/7\pi & n = 2 \\ 1/\pi & n = 3 \end{cases} \tag{9}$$

An illustration of an SPH smoothing kernel function in the three-dimensional case is shown in Fig. 1. Using the SPH approximations given in Eqs. 6 and 7 with Eq. 1, the Lagrangian description leads to

$$\frac{d\rho_i}{dt} = \rho_i \sum_{j=1}^N \frac{m_j}{\rho_j} (\mathbf{v}_i - \mathbf{v}_j) \nabla \phi_{ij} \tag{10}$$

where  $\phi_{ij} \equiv \phi_h(\mathbf{x}_i - \mathbf{x}_j)$ , and  $\mathbf{v} = d\mathbf{x}/dt$  is the velocity vector. The incompressible Navier–Stokes equations can be discretized as

$$\begin{aligned} \frac{d\mathbf{v}_i}{dt} = & - \sum_{j=1}^N m_j \left( \frac{p_i}{\rho_i^2} + \frac{p_j}{\rho_j^2} + \Pi_{ij} \right) \nabla \phi_{ij} \\ & + \mu \sum_{j=1}^N \frac{m_j}{\rho_j} (\mathbf{v}_i - \mathbf{v}_j) \nabla^2 \phi_{ij} + \frac{b_i}{\rho_i} \end{aligned} \tag{11}$$

where  $\Pi_{ij}$  is an artificial viscosity term, defined as

$$\Pi_{ij} = \begin{cases} \frac{Q_2 \mu_{ij}^2 - Q_1 c_{ij} \mu_{1j}}{\rho_{ij}} & \text{if } (\mathbf{v}_i - \mathbf{v}_j) \cdot (\mathbf{x}_i - \mathbf{x}_j) < 0 \\ 0 & \text{otherwise} \end{cases} \tag{12}$$

In the above equation,  $Q_1$  and  $Q_2$  are the linear and quadratic bulk viscosity coefficients, respectively,  $c_i$  is the speed of sound at  $\mathbf{x}_i$ ,  $\rho_{ij} = (\rho_i + \rho_j)/2$ ,  $\mu_{ij} = [h_{ij}(\mathbf{v}_i - \mathbf{v}_j) \cdot (\mathbf{x}_i - \mathbf{x}_j)] / [(\mathbf{x}_i - \mathbf{x}_j)^2 + 0.01h_{ij}]$ ,  $h_{ij} = (h_i + h_j)/2$ , and  $c_{ij} = (c_i + c_j)/2$  [57].

#### 4 ANCF approach

As previously mentioned, in studying the effect of liquid sloshing on vehicle dynamics and stability, the main concern is predicting the average time-varying fluid inertia forces. Simple rigid-body pendulum models are often used to obtain an estimate of the fluid inertia forces and their effect on the vehicle dynamics and stability. In this investigation, the continuum-based FE *absolute nodal coordinate formulation* (ANCF), which allows for developing a total Lagrangian non-incremental solution procedure suited for the nonlinear analysis of large-rotation and large-deformation problems, is used [69]. The ANCF method was originally developed for solving solid mechanics problems, but it has also been successfully applied for predicting the fluid average inertia properties in liquid sloshing problems. Wei et al. [78] developed a total Lagrangian continuum-based ANCF liquid sloshing formulation which can be systematically integrated with MBS algorithms. The ANCF liquid sloshing method addresses the deficiencies of the low-order continuum-based liquid sloshing formulation proposed by Wang et al. [77], which cannot describe large fluid displacements. ANCF liquid sloshing models were used by Shi et al. [72] with MBS railroad vehicle algorithms that allow for wheel/rail separation and by Nicolsen et al. [59] with a fully nonlinear tanker truck vehicle model. The validation of the ANCF liquid sloshing solution procedure was performed by Grossi and Shabana [27], who compared the results of this method with numerical and experimental data published in the literature. Grossi and Shabana [28] also generalized the continuum-based ANCF liquid sloshing approach to the analysis of non-Newtonian fluids and studied the effect of crude oil sloshing on railroad vehicle dynamics and stability.

In the ANCF description, the vector of element nodal coordinates includes both absolute position and gradient coordinates, allowing for describing arbitrarily complex fluid shapes and correctly capturing rigid-body motion. The use of position vector gradients as ANCF nodal coordinates allows for modeling the inter-

action between the fluid and the external environment in a straightforward manner; ensures the continuity of the gradient vectors and their time derivative, strains, and stresses at the nodal points; and leads to a constant mass matrix and zero centrifugal and Coriolis forces. Furthermore, because a small number of ANCF elements can be used to describe very complex fluid shapes, models with significantly fewer *degrees of freedom* (DOF) than what is required by other existing methods can be developed to achieve the same accuracy [27]. Because the ANCF liquid sloshing method is based on a total Lagrangian approach, the mesh moves with the fluid material points and allows for predicting the location of the fluid free surface with higher degree of accuracy. The ability to correctly capture highly deformed fluid shapes is necessary in order to have an accurate estimate of the fluid inertia forces. It is important to point out that in the case of severe mesh distortion, an adaptive mesh refinement algorithm should be used to prevent loss of the solution accuracy. Another important feature of the ANCF liquid sloshing method is that it can be systematically integrated with MBS solvers without the need for the use of a co-simulation approach. However, due to the use of a continuum-based Lagrangian mesh, the ANCF method does not capture turbulence, splashing effects, and the motion of solids through fluids.

The position field of an ANCF element  $j$  can be written as  $\mathbf{r}^j(\mathbf{x}^j, t) = \mathbf{S}^j(\mathbf{x}^j)\mathbf{e}^j(t)$ , where  $\mathbf{r}^j$  is the global position vector of an arbitrary point on the element  $j$ ,  $\mathbf{S}^j$  is the shape function matrix that depends on the element spatial coordinates  $\mathbf{x}^j = [x_1^j \ x_2^j \ x_3^j]^T$  and  $\mathbf{e}^j$  is the vector of time-dependent element nodal coordinates [69]. The vector of nodal coordinates of element  $j$  at node  $k$  is defined for a fully parameterized three-dimensional element as  $\mathbf{e}^j = \left[ (\mathbf{r}^{jk})^T \ (\mathbf{r}_{x_1}^{jk})^T \ (\mathbf{r}_{x_2}^{jk})^T \ (\mathbf{r}_{x_3}^{jk})^T \right]^T$ , where  $\mathbf{r}^{jk}$  is the absolute position vector of node  $k$  of the element  $j$  and  $\mathbf{r}_{x_l}^{jk}$  is the gradient vector obtained by differentiation with respect to the element spatial coordinates  $x_l$ ,  $l = 1, 2, 3$ . The use of the ANCF total Lagrangian formulation allows for simply writing the absolute acceleration vector as  $\mathbf{a}^j = \mathbf{S}^j\ddot{\mathbf{e}}^j$ , where  $\ddot{\mathbf{e}}^j$  is the second time derivative of the nodal coordinate vector  $\mathbf{e}^j$ . Similarly, the absolute velocity vector is defined as  $\mathbf{v}^j = \mathbf{S}^j\dot{\mathbf{e}}^j$ . The fluid partial differential equations of motion shown in Eq. 4 can be reduced to a set of second-order ordinary differential equations using the principle of virtual

work and the ANCF displacement field as

$$\mathbf{M}^j \ddot{\mathbf{e}}^j = \mathbf{Q}_b^j + \mathbf{Q}_t^j + \mathbf{Q}_C^j - \mathbf{Q}_P^j + \mathbf{Q}_v^j \quad (13)$$

where  $\mathbf{M}^j = \int_{V^j} \rho^j (\mathbf{S}^j)^T \mathbf{S}^j dV^j$  is a constant symmetric mass matrix,  $V^j$  is the element volume,  $\mathbf{Q}_b^j = \int_{V^j} (\mathbf{S}^j)^T \mathbf{b}^j dV^j$  is the vector of generalized body forces,  $\mathbf{Q}_t^j = \int_{s^j} (\mathbf{S}^j)^T \boldsymbol{\sigma}^j \mathbf{n}^j ds^j$  is the vector of generalized surface traction forces,  $s^j$  is the surface area,  $\mathbf{n}^j$  is the unit outward vector normal to  $s^j$ ,  $\mathbf{Q}_C^j = (\mathbf{S}^j)^T \mathbf{F}_C^j$  is the vector of generalized contact forces,  $\mathbf{F}_C^j$  is a penalty force vector,  $\mathbf{Q}_v^j = - \int_{V^j} 2\mu \left[ (\mathbf{C}_r^j)^{-1} \dot{\boldsymbol{\epsilon}}^j (\mathbf{C}_r^j)^{-1} \right] : (\partial \boldsymbol{\epsilon}^j / \partial \mathbf{e}^j) dV^j$  is the vector of generalized viscous forces,  $\mathbf{C}_r^j = (\mathbf{J}^j)^T \mathbf{J}^j$  is the right Cauchy–Green deformation tensor,  $\mathbf{J}^j$  is the matrix of position vector gradients,  $\boldsymbol{\epsilon}^j = 1/2 (\mathbf{C}_r^j - \mathbf{I})$  is the Green-Lagrange strain tensor,  $\mathbf{Q}_P^j = \int_{V^j} (\partial U^j / \partial \mathbf{e}^j) dV^j$  is the vector of generalized penalty forces, and  $U^j$  is a penalty strain energy function [27, 78].

## 5 Formulation differences

Based on the summary of the SPH and ANCF equations presented in the preceding two sections, the following basic differences between the two formulations can be identified:

1. The SPH formulation is a particle-based approach, while ANCF is a continuum-based approach. Particle kinematics is concerned with discrete points, while in a continuum approach, a distributed-matter description is used. Smoothing the region using splines or other polynomials or functions is not equivalent to using polynomial descriptions for elements with boundaries well defined by nodal points and geometries in the reference configuration. For this reason, the assumed kinematic descriptions are not same.
2. The SPH and ANCF approaches for describing the geometry in the reference configurations are fundamentally different. For ANCF elements, the matrix of position vector gradients in the reference configuration plays a fundamental role.
3. In the SPH approach, a nodal mass is predefined and used to formulate the inertia forces, which is equivalent to using a lumped-mass formulation. Such an

approach can be used to describe an arbitrarily large displacement. A diagonal lumped-mass matrix cannot, however, be used with ANCF elements since such a lumping scheme does not allow for correctly describing the rigid-body motion. A consistent mass formulation must be used with ANCF elements.

4. The interaction between the ANCF elements is defined using linear algebraic constraint equations, and this results in constraint (reaction) forces at the nodal points. The use of the constraint connectivity conditions does not require assuming penalty force coefficients. In the SPH approach, the interaction between particle-based regions is defined using a penalty formulation.
5. The use of the discrete inertia representation and the penalty contact formulation to describe the SPH particle interaction has the advantage of allowing for mesh distortions that cannot be conveniently captured using the continuum-based ANCF approach. This, however, comes at the expense of the need for much larger model dimensions that require larger array spaces and costly computational time.
6. The SPH and ANCF formulations of the elastic and/or viscous forces are not equivalent. Different kinematic descriptions are used in the two different approaches. Integration over the element volume and standard FE assembly procedure are required in the ANCF elastic and/or viscous force formulations, while summation over the number of particles is required for the SPH approach (Eq. 11). The standard FE assembly procedure is based on the algebraic connectivity conditions at the element nodes, and this ensures the continuity of the ANCF strains and stresses at the nodal points.

In the following section, a comparative study is performed based on numerical results obtained using the two fundamentally different approaches (SPH and ANCF). This comparative study sheds light on the accuracy and computational efficiency of the two approaches when used for solving liquid sloshing problems. The performance of the SPH particle-based approach and the ANCF continuum-based approach in different sloshing scenarios, and under different excitation conditions is evaluated.

## 6 Numerical results

In this section, two benchmark problems are considered to compare the performance of the ANCF and SPH methods and evaluate the wave breaking effect in liquid sloshing problems. The first benchmark problem is the dam break example [54,55], while the second benchmark problem is the sloshing tank example [19], in which liquid sloshing motion is generated in a rectangular tank subjected to horizontal excitation. In both problems, the fluid considered is water, which is assumed to have mass density and dynamic viscosity coefficients of  $1000 \text{ kg/m}^3$  and  $0.001 \text{ Pa} \cdot \text{s}$ , respectively. The SPH simulations are performed using the commercial software LS-DYNA, while the ANCF results are obtained using the general-purpose MBS software SIGMA/SAMS (Systematic Integration of Geometric Modeling and Analysis for the Simulation of Articulated Mechanical Systems). The numerical time integration methods used to solve the fluid equations of motion in case of the SPH and ANCF methods are the central difference scheme and the third-order Implicit Adams method [29], respectively. The simulations are performed on a computer with an Intel Core i7, 3.4 GHz processor and 8 GB RAM. For both benchmark problems, the convergence rates from the ANCF and SPH methods are studied and the CPU simulation times versus the number of degrees of freedom (DOF) are compared. The numerical errors in the convergence study are calculated using the *normalized root-mean square error* (NRMSE),  $e_n$ , defined as  $e_n = \sqrt{\sum_{i=1}^{N_m} (s_i^c - s_i^r)^2 / \sum_{i=1}^{N_m} (s_i^r)^2}$ , where  $s_i^c$  and  $s_i^r$  are the  $i$ th computed and reference data points, respectively, and  $N_m$  is the total number of data points.

### 6.1 Dam break benchmark problem

In the dam break problem, the fluid assumes an initially square configuration with side dimension  $H_w = 0.5 \text{ m}$ , as shown in Fig. 2. The column of fluid collapses over the rigid ground under the effect of gravity, and the position of the water front as a function of time is measured. Dam break flows are encountered in many industrial and environmental processes, and they are well suited for testing the capability of numerical methods of describing complex fluid free surface shapes. The ANCF solution is obtained using a mesh of rectangular ANCF elements, which have cubic shape functions

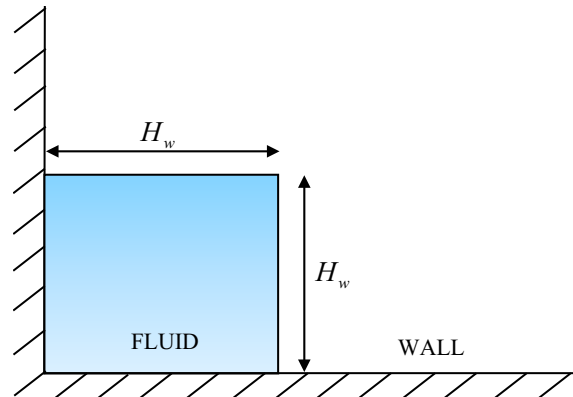


**Fig. 2** Schematic diagram of dam break problem

and 6 degrees of freedom per node [62]. Unilateral constraints at the contact interface with the rigid walls are introduced using the same penalty contact algorithm as described by Grossi and Shabana [27]. For the SPH model, the wall rigid boundaries are defined using four-noded Belytschko–Tsay shell elements, whereas the fluid is modeled using SPH nodes. The water constitutive model is defined using a “Null material” with Grüneisen equation of state [30,56]. The algorithm used to define the contact between the fluid and the rigid boundary is “Automatic Nodes to Surface” [52]. The numerical results and mesh convergence for this problem are presented in terms of the dimensionless time and position coordinates  $t^* = t\sqrt{g/H_w}$  and  $x^* = x_f/H_w$ , respectively, where  $g = 9.81 \text{ m/s}^2$  is the gravity constant and  $x_f$  is the position of the water front. The converged solution for each method is obtained by calculating the normalized error  $e_n$  between two successively refined meshes until  $e_n \leq 0.005$ . It is found that the converged solution can be obtained using a mesh of  $10 \times 10$  ANCF rectangular elements, while a grid of  $125 \times 125$  particles is required when using the SPH method. Figure 3 shows a comparison between the SPH and ANCF converged solutions, the experimental results produced by Martin and Moyce [54,55], and the analytical solution of Ritter [67]. It is clear that the SPH and ANCF solutions are in good agreement. The deviation from the experimental results is partly due to experimental uncertainties and partly to some physical effects which are not accounted for in the numerical results, such as the interaction between the fluid and surrounding air, as discussed in the literature [1,17,49]. The evolution of the fluid free surface and the horizontal

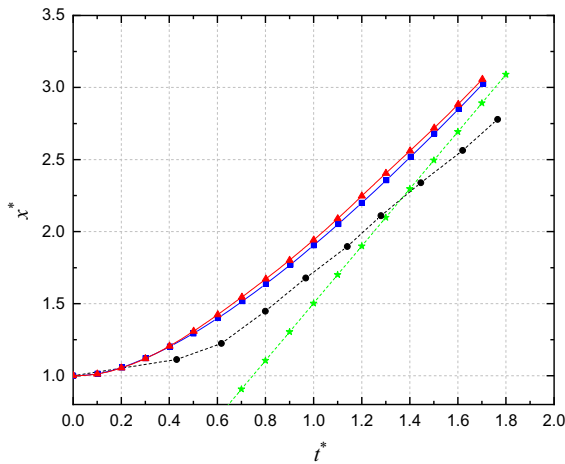


**Fig. 3** Wave front comparisons between ANCF, SPH, Ritter solutions, and experimental data (—▲— ANCF, —■— SPH, —★— Ritter, - -●- - experimental). (Color figure online)

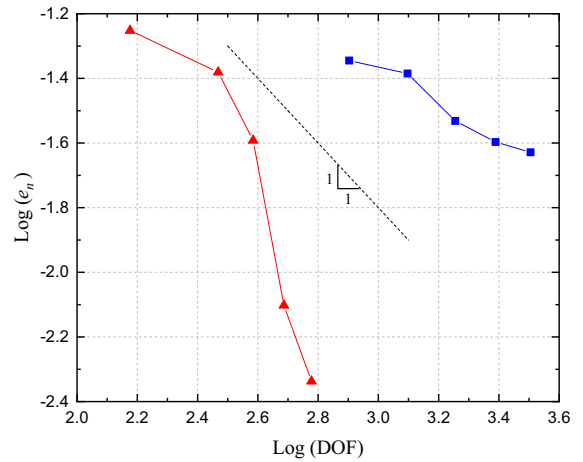
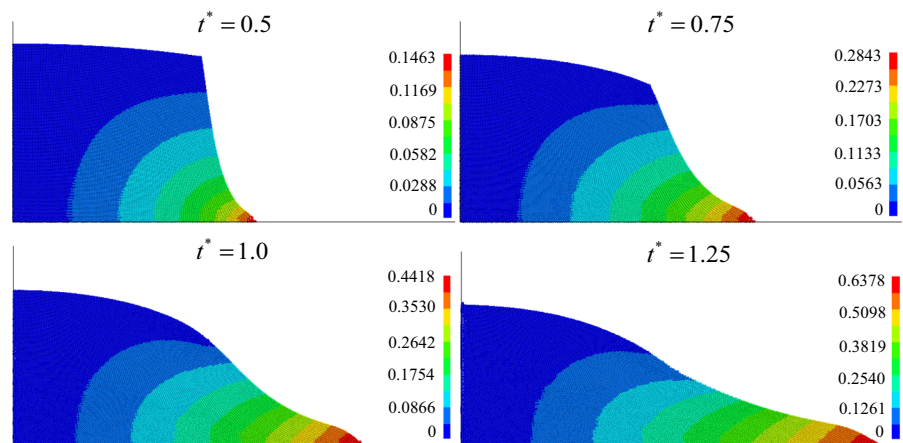


**Fig. 5** Convergence of the SPH and ANCF solutions for the dam break problem (—▲— ANCF, —■— SPH). (Color figure online)

displacement field are shown at different time instants in Fig. 4, while the convergence is presented in Fig. 5, which shows the normalized error  $e_n$  versus the number of degrees of freedom (DOF). The reference solutions used to calculate  $e_n$  for the ANCF and SPH methods are a mesh of  $10 \times 10$  rectangular ANCF elements and a grid of  $125 \times 125$  SPH particles, respectively. It is observed that the ANCF method has a faster convergence rate when compared to the SPH method for this problem. Furthermore, the number of degrees of freedom employed in the converged ANCF solution is nearly 35 times less than that required to obtain the SPH converged solution. Figure 6 shows the simulation time required by the ANCF and SPH models as the number

of degrees of freedom is increased. It is observed that the SPH and ANCF curves are almost parallel, indicating that the rate of increase in the CPU time resulting from mesh refinement is similar for both methods. It is interesting to notice that if nearly the same number of degrees of freedom is employed in both the ANCF and SPH models, the SPH approach requires less simulation time but leads to a significant deterioration of the solution accuracy. Furthermore, the CPU time required to obtain the ANCF converged solution is 70% less than the CPU time required by the converged SPH solution. The SPH and ANCF error and CPU time as a function of the model degrees of freedom are presented in Table 1.

**Fig. 4** SPH solution of the fluid deformed shape at different dimensionless times ( $125 \times 125$  particles; horizontal displacement is in meters). (Color figure online)





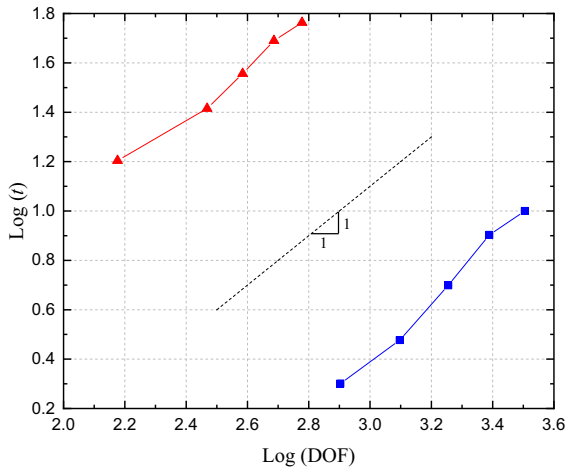


**Fig. 6** CPU time for the dam break problem (—▲— ANCF, —■— SPH). (Color figure online)

**Table 1** Normalized root-mean square error (NRMSE) and CPU time obtained for the broken dam problem

ANCF			SPH		
DOF	$e_n$	CPU time (s)	DOF	$e_n$	CPU time (s)
150	0.056	16	1800	0.0294	5
294	0.0416	26	3200	0.0235	10
384	0.0256	36	5000	0.0117	18
486	0.0079	49	9800	0.0053	68
600	0.0046	58	16200	0.0031	110
726 <sup>a</sup>	0	75	31250 <sup>a</sup>	0	284

<sup>a</sup>Reference solution

### 6.2 Sloshing tank benchmark problem

The initial configuration and geometry of the sloshing tank problem is shown in Fig. 7. This initial configuration is based on the experiment of Faltinsen and Timokha [19], where the tank length is  $L_t = 1.73$  m, the water depth is  $H_w = 0.6$  m, and the tank height is  $H_t = 1.15$  m. The horizontal harmonic tank motion is defined as  $x_t = A \cos(2\pi t/T)$ , where  $x_t$  is the location of the tank, and  $A = 0.032$  m and  $T = 1.5$  s are, respectively, the amplitude and period of oscillation. Numerical simulations are performed to compute the value of  $H_w$  at a measurement point  $P_m$ , located 0.05 m away from the left tank wall. The ANCF solution is obtained using a mesh of ANCF brick (solid) elements, which have cubic shape functions and 12 degrees of freedom per node [63]. The rigid rectangular

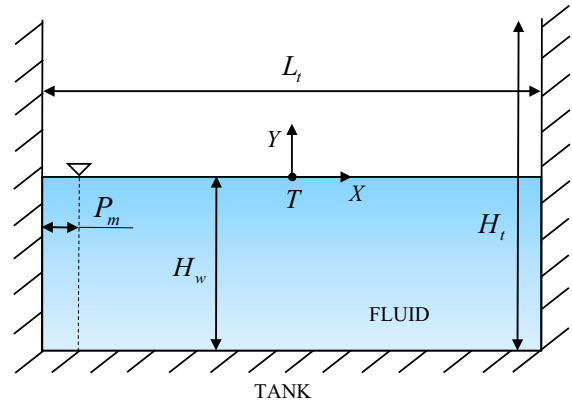


**Fig. 7** Schematic diagram of the sloshing tank problem

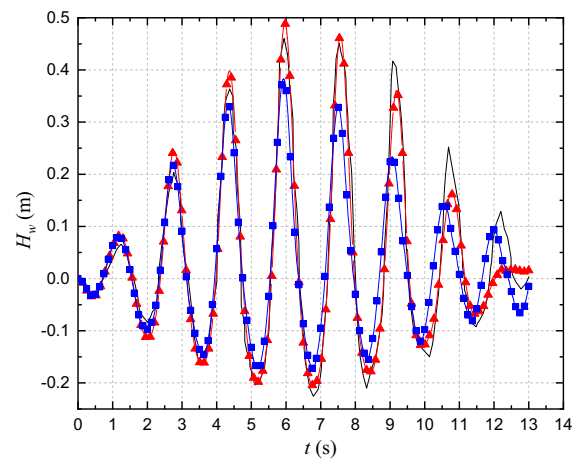
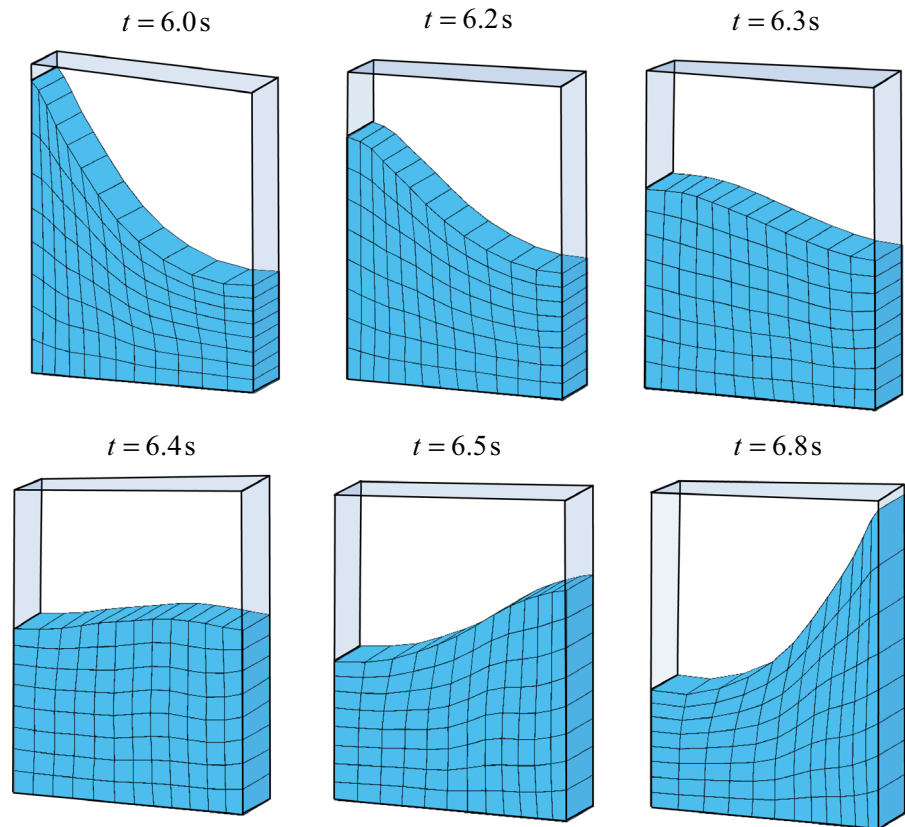


**Fig. 8** Wave height predicted using different methods (—▲— ANCF, —■— SPH, — experimental). (Color figure online)

tank is modeled using the ANCF reference node [68]. The SPH model is developed using the procedures and assumptions previously described in this section. Figure 8 shows the wave height measured at the measurement point using a  $12 \times 8$  ANCF mesh and a  $340 \times 120$  SPH grid. Overall, the numerical results agree well with the experimental data in terms of both amplitude and frequency of oscillation. The smaller peak amplitudes predicted using the SPH method can be explained considering that the SPH solid boundary conditions require a specialized treatment in order to obtain suitable repulsive forces [71]. The fluid deformed shape at different time instants calculated using the ANCF method is shown in Fig. 9. The normalized error  $e_n$  calculated with respect to the set of experimental data provided by

**Fig. 9** ANCF solution of the fluid deformed shape



Faltinsen and Timokha [19] and the simulation times are shown in Table 2. In agreement with the results obtained for the dam break problem, the ANCF solution, using 1932 degrees of freedom, can be obtained using nearly 40 times fewer coordinates than the number of coordinates required to obtain the SPH solution (81600 coordinates). Furthermore, the CPU time required to obtain the ANCF solution is nearly 25% less than that required to obtain the SPH solution, as reported in Table 2. Figure 10 shows the position of the fluid center of mass calculated with respect to the geometric center of the tank. Overall, the numerical results are in good agreement with the experimental data. It is observed that the SPH method underpredicts the oscillations in the location of the center of mass as compared to experimental measurement. With regard to the convergence characteristic of each method, Fig. 11 shows that the convergence rate of the ANCF method is slower than the SPH one. Figure 12 shows the simulation time obtained using the ANCF and SPH methods as a function of mesh refinement. In agreement with the results obtained for the dam break problem, the rate of increase

**Table 2** Normalized root-mean square error (NRMSE) and CPU time obtained for the sloshing tank problem

ANCF			SPH		
DOF	$e_n$	CPU time (s)	DOF	$e_n$	CPU time (s)
708	0.2754	1632	5400	0.6253	389
960	0.2437	3000	9600	0.5219	955
1248	0.2358	6463	21000	0.4386	2919
1572	0.2234	9335	58000	0.3908	12929
1932	0.1903	16793	81600	0.3864	21899

in CPU time resulting from mesh refinement is similar for both methods.

### 6.3 Breaking wave effect

In this section, the effect of breaking waves on liquid sloshing dynamics is studied. As the result of sloshing motion, turbulent regions can develop in the fluid and at the interface between the fluid and the

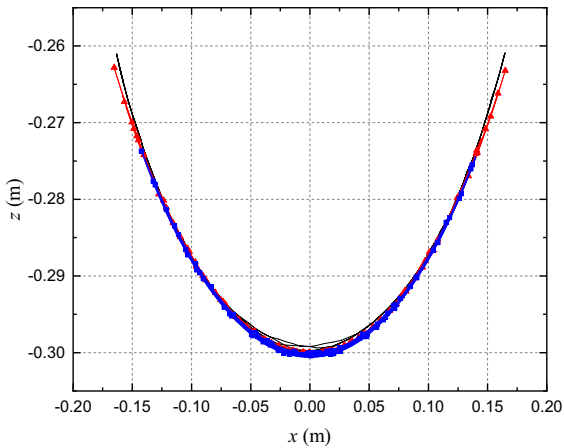


**Fig. 10** Position of the fluid center of mass (—▲— ANCF, —■— SPH, — experimental). (Color figure online)

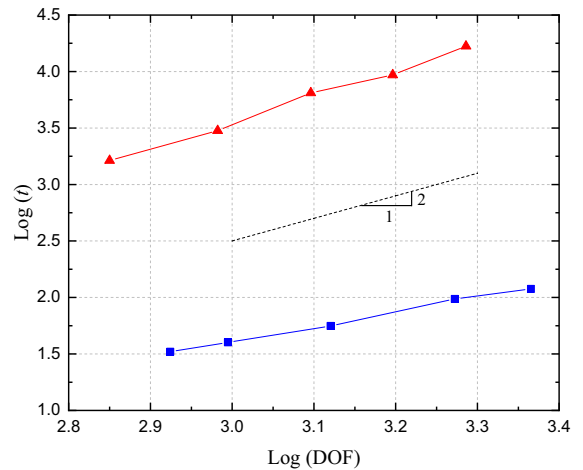


**Fig. 12** CPU time for the sloshing tank problem (—▲— ANCF, —■— SPH). (Color figure online)

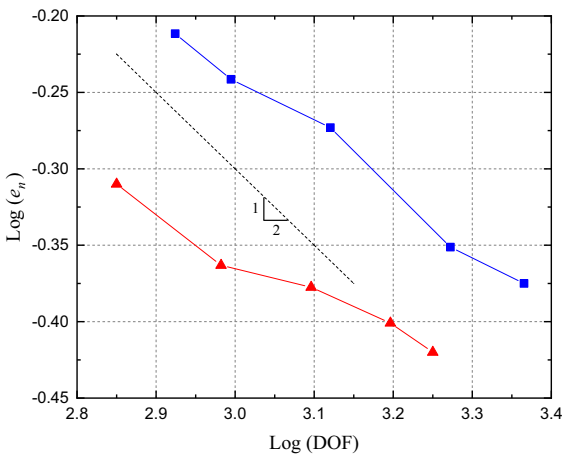


**Fig. 11** Convergence of the SPH and ANCF solutions for the sloshing tank problem (—▲— ANCF, —■— SPH). (Color figure online)

container. These regions, which are characterized by irregular fluid fluctuations and mixing, can be accurately captured using Eulerian-based methods or mesh-free Lagrangian formulations, such as SPH. On the other hand, the continuum-based ANCF method cannot be used to capture vortices and wave breaking phenomena. Figure 13 shows localized turbulent regions obtained for the sloshing tank problem described in Sect. 6.2, using the SPH method. For the sloshing scenario considered in Sect. 6.2, the effect of turbulence is negligible, and the results obtained using the ANCF method are in good agreement with the experimental and SPH results. In order to initiate significant turbu-

lence motion, the period and amplitude of excitation of the tank in the sloshing tank problem are changed. Using the values of the excitation amplitude, namely  $A = 0.032$  m,  $0.084$  m,  $0.136$  m, three different turbulence scenarios are defined as *light*, *moderate* and *severe*, respectively. For each value of excitation amplitude, the effect of varying the excitation frequency on liquid sloshing dynamics is investigated. The time histories of the fluid free surface shape obtained at different time instants for the moderate and severe turbulent scenarios are shown in Figs. 14 and 15, respectively. It is clear that while in the moderate turbulence case the turbulent regions are mainly confined to the fluid free surface, in case of severe turbulence, vortical flows are generated within the entire fluid volume. Figure 16 shows the  $x$ -displacement of the fluid center of mass obtained using the ANCF and SPH methods for each turbulent scenario considering three different values of excitation frequency  $\omega_e = 1.12\omega_0$ ,  $1.48\omega_0$ ,  $2.22\omega_0$ , where  $\omega_0 = 0.6$  Hz is the first frequency of the free oscillations. The sloshing oscillation frequency can be calculated for a rectangular tank using the analytical relationship  $\omega_n^2 = gk_n \tanh(k_n H_w)$ , where  $\omega_n$  is the  $n$ th sloshing oscillation frequency,  $g$  is the gravity constant,  $k_n = (2n + 1)\pi/L_t$  is the wave number, and  $n$  is the sloshing mode number [18,21,50,51,73,80]. It is important to point out that the equation  $\omega_n^2 = gk_n \tanh(k_n H_w)$  is valid under the assumptions of inviscid, incompressible, irrotational flow and negligible surface tension. Figure 16 shows that in the case of light and moderate turbulence, the ANCF and SPH

**Fig. 13** Small turbulent regions obtained using the SPH method

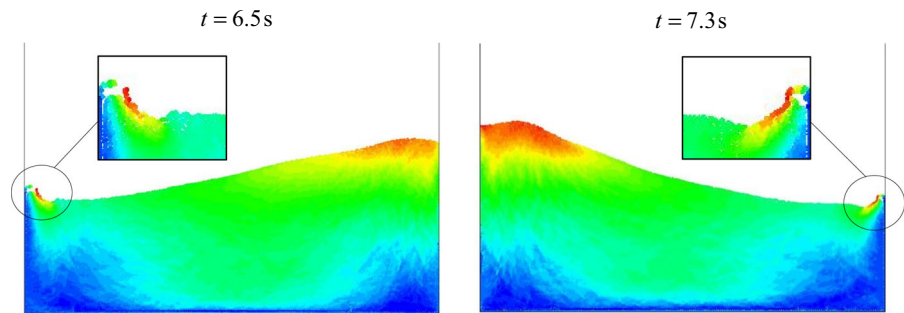
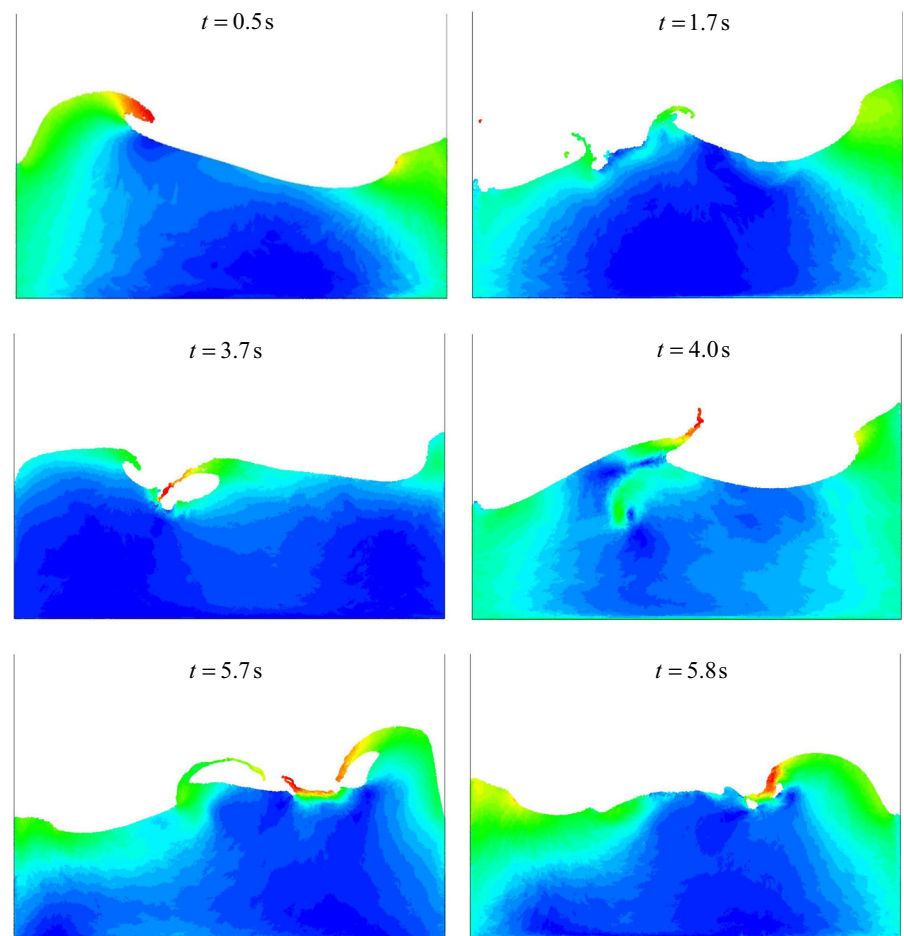


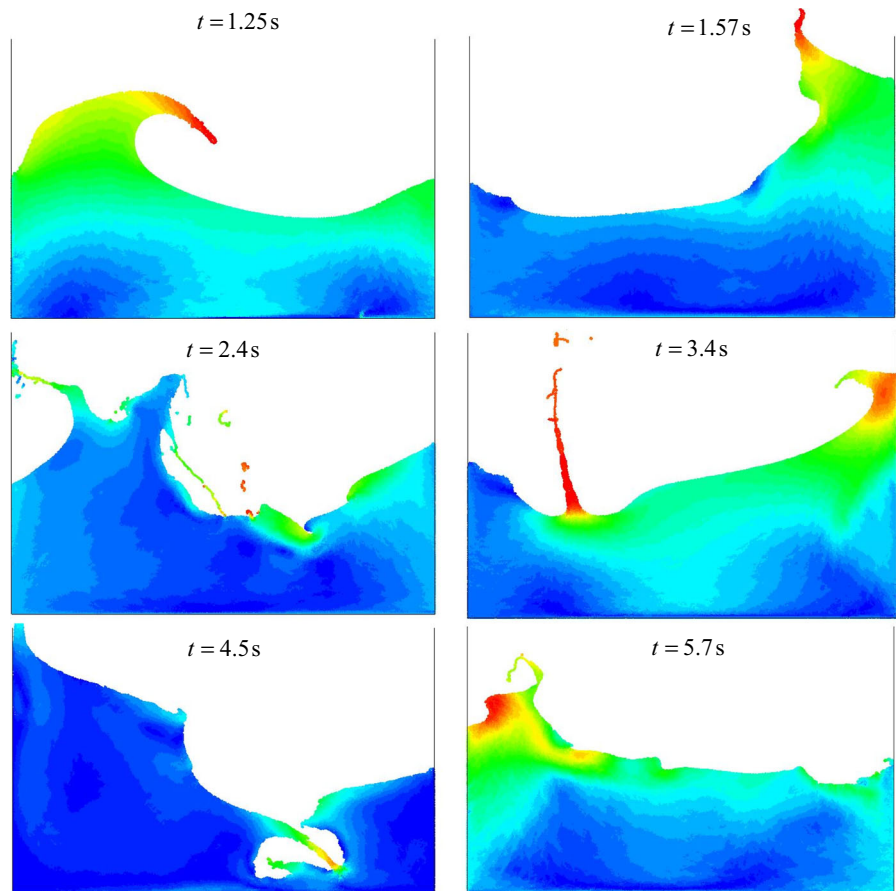
**Fig. 14** SPH prediction of the moderate turbulence scenario ( $A = 0.084$  m,  $T = 0.75$  s)



solutions are in good agreement. These results show that the ANCF continuum-based method is capable of accurately averaging the fluid inertia properties, thus leading to an accurate calculation of the position of the fluid center of mass. As the effects of the breaking waves increase, the ANCF method does not capture the increase in mechanical energy dissipation; and

the amplitude of the fluid oscillation computed using the ANCF method overpredicts the SPH solution. This behavior is observed mainly in the case of moderate turbulence with excitation frequency  $\omega_e = 2.22\omega_0$ , and in the three severe turbulent scenarios with  $A = 0.136$  m. The maximum  $x$ -displacement of the fluid center of mass as a function of the frequency ratio

**Fig. 15** SPH prediction of the severe turbulence scenario ( $A = 0.136$  m,  $T = 1.125$  s)



$\omega_e/\omega_0$  is shown for the light, moderate, and severe turbulent scenarios in Figs. 17, 18 and 19, respectively. The maximum  $x$ -displacement of the fluid center of mass is normalized with respect to the value of maximum  $x$ -displacement obtained in the case of excitation frequency  $\omega_e = 0.5$  Hz. The  $x$ -position of the fluid center of mass can be calculated analytically using the asymptotic nonlinear multimodal approach as  $x_C(t) = -2/\pi^2 h^* \sum_{i=1}^{n_f} \beta_i(t) \frac{1}{i^2} (1 + (-1)^{i+1})$ , where  $h^* = 2H_w/L_t$ ,  $n_f$  is the number of Fourier terms,  $\beta_i$  is a generalized modal coordinate, and  $t$  is time [19–21]. It is important to point out that the use of the preceding equation for  $x_C$  is limited to the case of small fluid response amplitude to fluid depth ratio and in the case of negligible wave breaking effects. From the results shown in Fig. 17, it is clear that in the case of light turbulence, the ANCF and SPH results agree well with the analytical solution. Figure 18 shows that in case of moderate turbulence, a good agreement is observed between the SPH and ana-

lytical solutions, while the ANCF solution deviates from the reference solution as the excitation frequency increases. In case of severe turbulence, the asymptotic nonlinear multimodal approach cannot be used, and the SPH results are considered as the reference solution. In agreement with the results obtained for the moderate turbulent scenario, the ANCF solution shown in Fig. 19 deviates from the reference SPH solution as the excitation frequency increases. The non-monotonic behavior of the ANCF curves shown in Figs. 18 and 19 is expected because the ANCF method does not account for the energy dissipation due to the wave breaking. In order to identify the frequencies of the fundamental modes of displacement and the contribution of each mode to the sloshing response, the power spectral density associated with the results shown in Fig. 16 is calculated using the fast Fourier transform (FFT). The power spectrum  $S(\omega)$  is calculated considering three different levels of excitation frequency  $\omega_e = 1.12\omega_0$ ,  $1.48\omega_0$ ,  $2.22\omega_0$ , and three excita-

**Fig. 16**  $x$ -displacement of the fluid center of mass for different excitation frequencies and amplitudes (— ANCF, —●— SPH). (Color figure online)

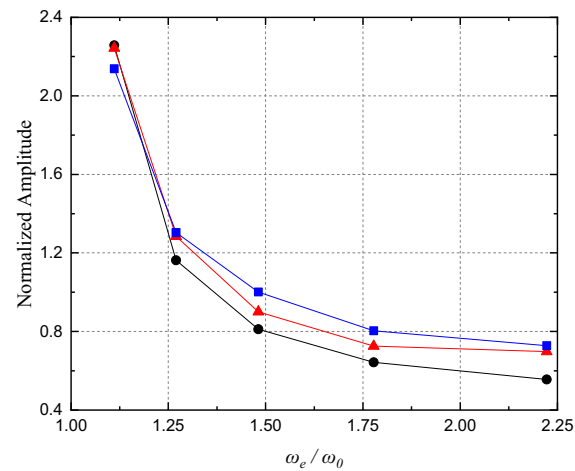
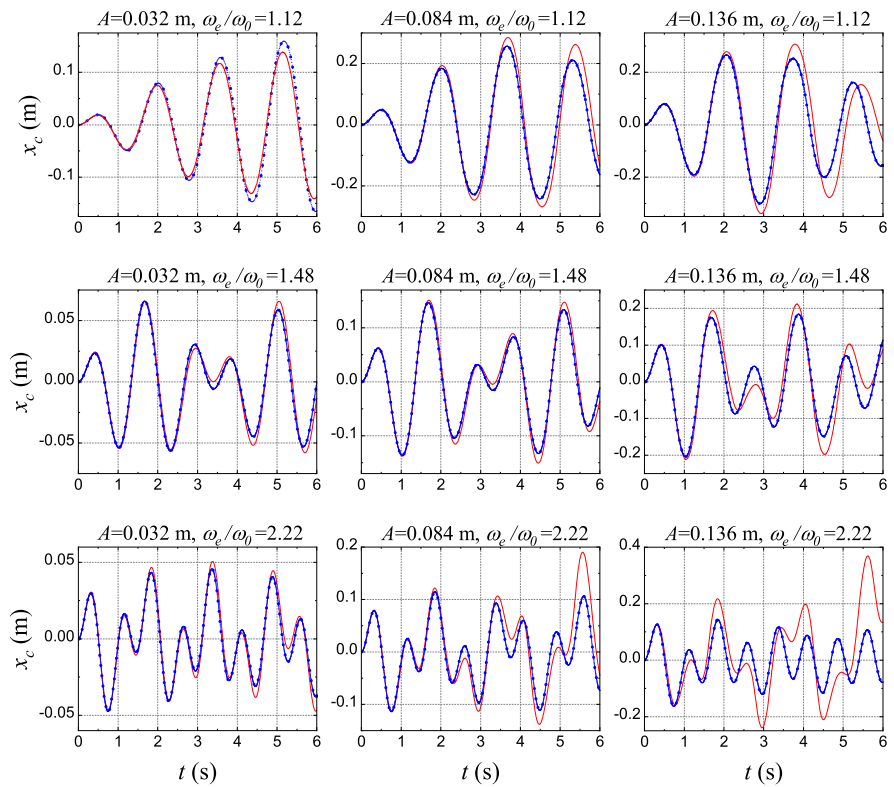


**Fig. 17** Normalized maximum amplitude of the fluid center of mass for  $A = 0.032$  m (—▲— ANCF, —■— SPH, —●— analytical). (Color figure online)

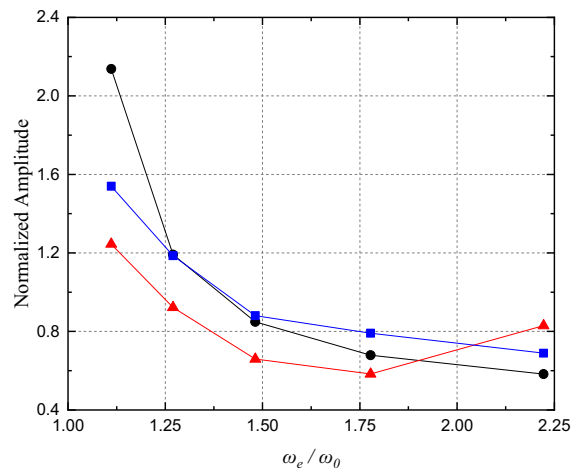


**Fig. 18** Normalized maximum amplitude of the fluid center of mass for  $A = 0.084$  m (—▲— ANCF, —■— SPH, —●— analytical). (Color figure online)

tion amplitudes  $A = 0.032$  m,  $0.084$  m,  $0.136$  m. Figure 20 shows the power spectrum based on the results obtained in the first 6 seconds of simulation. It is observed that when the excitation frequency is close to the fundamental frequency, i.e.,  $\omega_e = 1.12\omega_0$ ,

the sloshing response is dominated by the fundamental sloshing mode  $\omega_0$ . When the excitation frequency is larger than the fundamental frequency, i.e.,  $\omega_e = 1.48\omega_0$  and  $\omega_e = 2.22\omega_0$ , two dominant frequencies, namely the excitation frequency  $\omega_e$  and

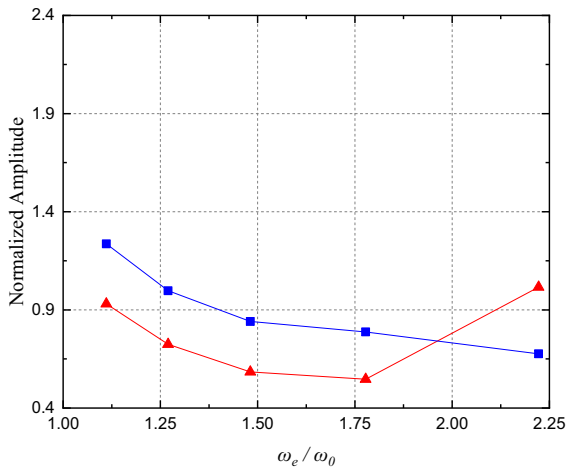
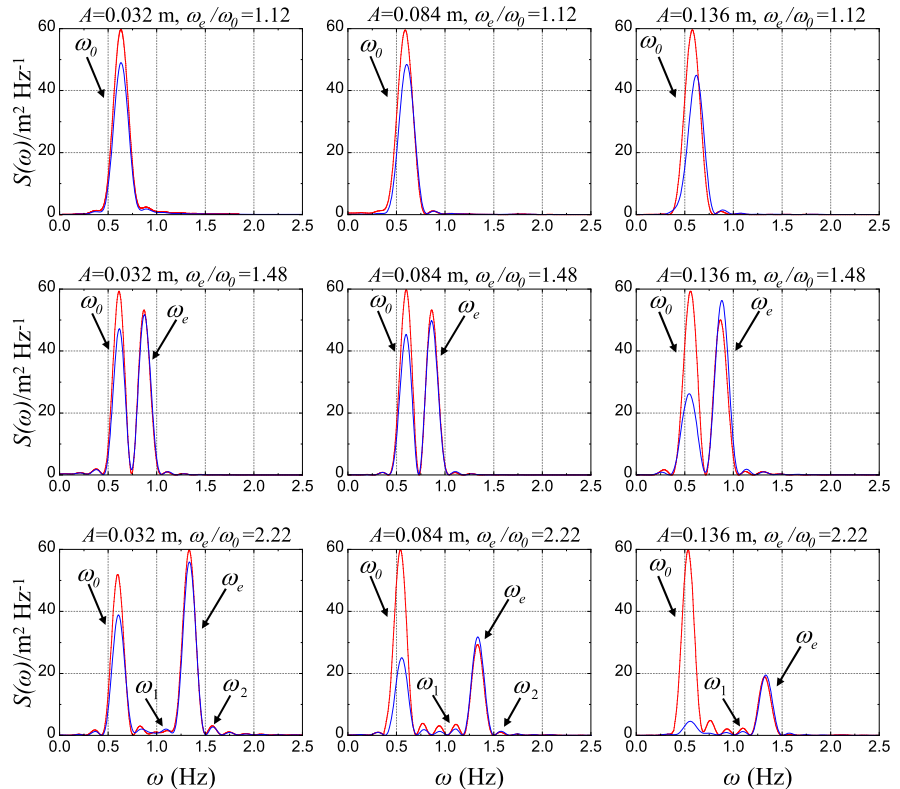


**Fig. 19** Normalized maximum amplitude of the fluid center of mass for  $A = 0.136$  m (—▲— ANCF, —■— SPH). (Color figure online)

the frequency  $\omega_0$ , can be identified. In the case of excitation frequency  $\omega_e = 2.22\omega_0$ , the responses at the higher sloshing oscillation frequencies  $\omega_1$  and  $\omega_2$  are also visible. It is observed that by increasing the excitation amplitude, the mechanical energy dissipa-

**Fig. 20** Power spectrum of the sloshing response (— ANCF, — SPH). (Color figure online)



tion due to the wave breaking significantly affects the energy content of the sloshing modes associated with the sloshing oscillation frequencies. Consequently, the transient response of the fluid is rapidly damped out when the SPH method is used, while it remains in the ANCF solution. The use of the ANCF method, which does not account for the hydrodynamic damping effects due to the wave breaking, leads to overpredicting the energy of the fundamental sloshing mode. On the other hand, a good agreement is found between the ANCF and SPH methods in predicting the stable steady-state fluid response associated with the excitation frequency. In the case of excitation amplitude  $A = 0.084$  m, the effect of the excitation frequency on the hydrodynamic loads is studied. Figure 21 shows the variation of the hydrodynamic force acting on the container at different levels of excitation frequency. In Fig. 21, the value of the hydrodynamic force is normalized with respect to the fluid mass. It is observed that as the excitation frequency gets closer to the fundamental sloshing oscillation frequency, the value of the hydrodynamic load increases. However, the wave breaking effects resulting from an increase in the excitation frequency do not

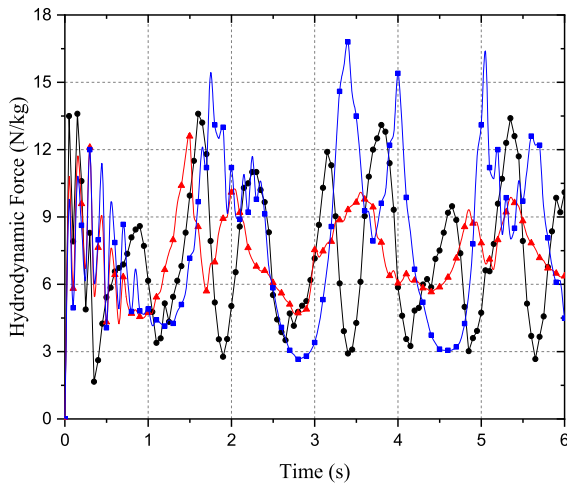


**Fig. 21** Hydrodynamic load calculated using the SPH method ( $\square$   $\omega_e/\omega_0 = 2.22$ ,  $\triangle$   $\omega_e/\omega_0 = 1.48$ ,  $\bullet$   $\omega_e/\omega_0 = 1.12$ ). (Color figure online)

lead to an increase in the maximum value of the hydrodynamic force.

## 7 Conclusion

This paper is focused on the study of breaking wave effects in liquid sloshing problems using the ANCF and SPH methods. The fundamental differences between the two formulations are presented, and the advantages and limitations of each method are discussed. The dam break and sloshing tank benchmark problems are used to assess the performance of both formulations in capturing the fluid dynamic behavior resulting from sloshing excitations. In the dam break problem, a good agreement is observed between the ANCF and SPH converged solutions. Moreover, it is found that the ANCF converged solution requires 35 times fewer degrees of freedom than the SPH solution. In the sloshing tank problem, while the ANCF solution agrees well with the experimental results, it is found that the SPH solution underpredicts the amplitude of the wave height at the point of interest and the lateral displacement of the fluid center of mass. In agreement to what is found for the dam break problem, the ANCF solution requires nearly 40 times fewer degrees of freedom as compared to the SPH solution. In case of the dam break problem, the CPU time required by the ANCF method to converge to the reference solution is 70% less than that required by the SPH method; in the slosh-

ing tank problem, the CPU time saving obtained using the ANCF method is 25%. In both benchmark problems, it is observed that the rate of increase in simulation time resulting from mesh refinement is comparable when the ANCF and SPH methods are used. The effects of breaking waves on liquid sloshing dynamics are investigated for the sloshing tank problem by varying the excitation frequency and amplitude. It is shown that in the case of light and moderate turbulence, the continuum-based ANCF method leads to an accurate prediction of the position of the fluid center of mass by averaging the fluid inertia properties. In case of severe turbulence, the mechanical energy dissipation due to vortical flows and wave breaking, which is not captured using the ANCF method, leads to damping out the fluid response. Severe sloshing scenarios, which cannot be captured using the ANCF method, can be accurately described using the particle-based SPH formulation.

It is important to point out that because of the use of two fundamentally different algorithms in the ANCF and SPH model simulations, less weight should be given to the CPU time comparison, while more weight should be given to the number of degrees of freedom of the models. This is mainly due to the fact that different optimization and parallelization methods are used in the two software employed in this study. Future investigations will focus on the study of fundamental sloshing issues, some of which are discussed in more recent investigations [36,37].

**Acknowledgements** This research was supported by the National Science Foundation (Project # 1632302).

### Compliance with ethical standards

**Conflict of interest** The authors declare that they have no conflict of interest.

## References

1. Abdolmaleki, K., Thiagarajan, K.P., Morris-Thomas, M.T.: Simulation of the dam break problem and impact flows using a Navier-Stokes solver. *Simulations* **13**, 17 (2004)
2. Beissel, S., Belytschko, T.: Nodal Integration of the element-free Galerkin method. *Comput. Methods Appl. Mech. Eng.* **139**, 49–71 (1996)
3. Belytschko, T., Guo, Y., Liu, W.K., Xiao, S.P.: A unified stability analysis of meshless particle methods. *Int. J. Numer. Methods Eng.* **48**, 1359–1400 (2000)
4. Belytschko, T., Krongauz, Y., Dolbow, J., Gerlach, C.: On the completeness of the meshfree particle methods. *Int. J. Numer. Methods Eng.* **43**(5), 785–819 (1998)



5. Belytschko, T., Krongauz, Y., Organ, D., Fleming, M., Krysl, P.: Meshless methods: an overview and recent developments. *Comput. Methods Appl. Mech. Eng.* **139**(1–4), 3–47 (1996)
6. Benz, W., Asphaug, E.: Impact simulations with fracture: I. Method and tests. *Icarus* **1233**, 98–116 (1994)
7. Benz, W., Asphaug, E.: Simulations of brittle solids using smoothed particle hydrodynamics. *Comput. Phys. Commun.* **87**, 253–265 (1995)
8. Bogaert, H., Kaminski, M.L., Brosset, L.: Full and large scale wave impact tests for a better understanding of sloshing: results of the sloshel project. In: *Proceedings ASME 30th Conference Ocean, Offshore and Arctic Engineering (OMAE)*, Rotterdam, The Netherlands, OMAE2011-49992, p. 11 (2011)
9. Bonet, J., Lok, T.S.: Variational and momentum preservation aspects of smooth particle hydrodynamic formulation. *Comput. Methods Appl. Mech. Eng.* **180**, 97–115 (1999)
10. Bouscasse, B., Colagrossi, A., Souto-Iglesias, A., Cercosa-Pita, J.L.: Mechanical energy dissipation induced by sloshing and wave breaking in a fully coupled angular motion system, I: theoretical formulation and numerical investigation. *Phys. Fluids* **26**(033103), 21 (2014)
11. Bredmose, H., Peregrine, D.H., Bullock, G.N.: Violent breaking wave impacts, part 2: modelling the effect of air. *J. Fluid Mech.* **641**, 389–430 (2009)
12. Bullock, G.N., Obhrai, C., Peregrine, D.H., Bredmose, H.: Violent breaking wave impacts. Part 1: results from large-scale regular wave tests on vertical and sloping walls. *Coast. Eng.* **54**(8), 602–617 (2007)
13. Chen, J.K., Beraun, J.E.: A generalized smoothed particle hydrodynamics method for nonlinear dynamic problems. *Comput. Methods Appl. Mech. Eng.* **190**, 225–239 (2000)
14. Chen, J.K., Beraun, J.E., Carney, T.C.: A corrective smoothed particle method for boundary value problems in heat conduction. *Int. J. Numer. Methods Eng.* **46**, 231–252 (1999)
15. Cho, J.R., Lee, H.W.: Nonlinear finite element analysis of large amplitude sloshing flow in two-dimensional tank. *Int. J. Numer. Methods Eng.* **61**, 514–531 (2004)
16. Colagrossi, A., Colicchio, G., Lugni, C., Brocchini, M.: A study of violent sloshing wave impacts using an improved SPH method. *J. Hydraul. Res.* **48**, 94–104 (2010)
17. Colagrossi, A., Landrini, M.: Numerical simulation of interfacial flows by smoothed particle hydrodynamics. *J. Comput. Phys.* **191**, 448–475 (2003)
18. Faltinsen, O.M.: A numerical non-linear method of sloshing in tanks with two-dimensional flow. *J. Ship Res.* **18**(4), 224–241 (1978)
19. Faltinsen, O.M., Timokha, A.N.: Multidimensional modal analysis of nonlinear sloshing in a rectangular tank with finite water depth. *J. Fluid Mech.* **407**, 201–234 (2000)
20. Faltinsen, O.M., Timokha, A.N.: Asymptotic modal approximation of nonlinear resonant sloshing in a rectangular tank with small fluid depth. *J. Fluid Mech.* **470**, 319–357 (2002)
21. Faltinsen, O.M., Timokha, A.N.: *Sloshing*. Cambridge University Press, Cambridge (2009)
22. Gingold, R.A., Monaghan, J.J.: Smoothed particle hydrodynamics: theory and application to non-spherical stars. *Mon. Not. R. Astron. Soc.* **181**, 375–389 (1977)
23. Gotoha, H., Khayyera, A., Ikari, H.: On enhancement of incompressible SPH method for simulation of violent sloshing flows. *Appl. Ocean Res.* **46**, 104–115 (2014)
24. Gray, J., Monaghan, J.J., Swift, R.P.: SPH elastic dynamics. *Comput. Methods Appl. Mech. Eng.* **190**, 6641–6662 (2001)
25. Gray, J.A., Monaghan, J.J.: Numerical modelling of stress fields and fracture around magma chambers. *J. Volcanol. Geothermal. Res.* **135**, 259–283 (2004)
26. Grenier, N., Antuono, M., Colagrossi, A., Le Touze, D., Alessandrini, B., Le Touzé, D.: An hamiltonian interface SPH formulation for multi-fluid and free surface flows. *J. Comput. Phys.* **228**(22), 8380–8393 (2009)
27. Grossi, E., Shabana, A.A.: Validation of a total lagrangian ANCF solution procedure for fluid–structure interaction problems. *J. Verif. Uncertain. Quantif.* **2**(4), 041001-1-041001-13 (2017)
28. Grossi, E., Shabana, A.A.: ANCF analysis of the crude oil sloshing in railroad vehicle systems. *J. Sound Vib.* **433**, 493–516 (2018)
29. Grossi, E., Shabana, A.A.: Analysis of high-frequency ANCF modes: Navier-Stokes physical damping and implicit numerical integration. *Acta Mech* (2019). <https://doi.org/10.1007/s00707-019-02409-8>
30. Grüneisen, E.: Theorie des Festen Zustandes Einatomiger Elemente. *Ann. Phys.* **344**(12), 257–306 (1912)
31. Hosain, M.L., Sand, U., Bel Fdhila, R.: Numerical investigation of liquid sloshing in carrier ship fuel tanks. *IFAC Pap.* **51**, 583–588 (2018)
32. Hu, X.Y., Adams, N.A.: A multi-phase SPH method for macroscopic and mesoscopic flows. *J. Comput. Phys.* **213**(2), 844–861 (2006)
33. Hu, Z.Z., Mai, T., Greaves, D., Raby, A.: Investigations of offshore breaking wave impacts on a large offshore structure. *J. Fluids Struct.* **75**, 99–116 (2017)
34. Ibrahim, R.A., Pilipchuk, V.N., Ikeda, T.: Recent advances in liquid sloshing dynamics. *Appl. Mech. Rev.* **54**(2), 133–199 (2001)
35. Ibrahim, Raouf A.: *Liquid Sloshing Dynamics: Theory and Applications*. Cambridge University Press, Cambridge (2005)
36. Ibrahim, R.A.: Recent advances in physics of fluid parametric sloshing and related problems, ASME. *J. Fluids Eng.* (2015). <https://doi.org/10.1115/1.4029544>
37. Ibrahim, R.A., Singh, B.: Assessment of ground vehicle tankers interacting with liquid sloshing dynamics. *Int. J. Heavy Veh. Syst.* **25**(1), 23–112 (2018)
38. Iglesias, A.S., Rojas, L.P., Rodriguez, R.Z.: Simulation of anti-roll tanks and sloshing type problems with smoothed particle hydrodynamics. *Ocean Eng.* **31**, 1169–1192 (2004)
39. Kim, J.W., Shin, Y.S., Bai, K.J.: A finite-element computation for the sloshing motion in LNG tank. *ABS technical papers* (2002)
40. Kim, Y.: Numerical simulation of sloshing flows with impact load. *Appl. Ocean Res.* **23**, 53–62 (2001)
41. Kim, Y., Shin, Y.S., Lee, K.H.: Numerical study on slosh-induced impact pressures on 3-D prismatic tanks. *Appl. Ocean Res.* **26**, 213–226 (2004)
42. Li, S., Liu, W.K.: *Meshfree Particle Methods*. Springer, Berlin (2007)
43. Libersky, L.D., Petschek, A.G.: Smooth particle hydrodynamics with strength of materials. In: *Trease, H.E., Fritts,*

- M.J., Crowley, W.P. (eds.) *Advances in the Free-Lagrange Method*, pp. 248–257. Springer, Berlin (1991)
44. Lin, P., Liu, P.L.F.: A numerical study of breaking waves in the surf zone. *J. Fluid Mech.* **359**, 239–264 (1998)
  45. Liu, G.R., Liu, M.B.: *Smoothed Particle Hydrodynamics: A Meshfree Particle Method*. World Scientific, Singapore (2003)
  46. Liu, D.M., Lin, P.Z.: A numerical study of three-dimensional liquid sloshing in tanks. *J. Comput. Phys.* **227**, 3921–3939 (2008)
  47. Liu, D.M., Lin, P.Z.: Three-dimensional liquid sloshing in a tank with baffles. *Ocean Eng.* **36**, 202–212 (2009)
  48. Liu, M.B., Feng, D.L., Guo, Z.M.: *A Modified SPH Method for Modeling Explosion and Impact Problems*. APCOM & ISCM, Wroclaw (2013)
  49. Lobovsky, L., Botia-Vera, E., Castellana, F., Mas-Soler, J., Souto-Iglesias, A.: Experimental investigation of dynamic pressure loads during dam break. *J. Fluids Struct.* **48**, 407–434 (2014)
  50. Love, J.S., Tait, M.J.: Equivalent linearized mechanical model for tuned liquid dampers of arbitrary tank shape. *J. Fluids Eng.* **133**(6), 061105 (2011)
  51. Love, J.S., Tait, M.J.: Linearized sloshing model for 2D tuned liquid dampers with modified bottom geometries. *Can. J. Civ. Eng.* **41**(2), 106–117 (2013)
  52. LS-DYNA<sup>®</sup> Keyword User's Manual—LSTC (2018)
  53. Lucy, L.B.: A numerical approach to the testing of the fission hypothesis. *Astronom. J.* **82**, 1013 (1977)
  54. Martin, J.C., Moyce, W.J.: An experimental study of the collapse of liquid columns on a rigid plane. *Philos. Trans. R. Soc. Lond. Ser. A* **244**, 312–324 (1952)
  55. Martin, J.C., Moyce, W.J.: Part IV—an experimental study of the collapse of liquid columns on a rigid horizontal plane. *Philos. Trans. R. Soc. Lond. A Math. Phys. Eng. Sci.* **244**(882), 312–324 (1952)
  56. Mie, G.: Zur kinetischen Theorie der Einatomigen Körper. *Ann. Phys.* **316**(8), 657–697 (1903)
  57. Monaghan, J.J., Poinracic, H.: Artificial viscosity for particle methods. *Appl. Numer. Math.* **1**(3), 187–194 (1985)
  58. Monaghan, J.J., Rafiee, A.: A simple SPH algorithm for multi-fluid flow with high density ratios. *Int. J. Numer. Methods Fluids* **71**, 537–561 (2013)
  59. Nicolsen, B., Wang, L., Shabana, A.: Nonlinear finite element analysis of liquid sloshing in complex vehicle motion scenarios. *J. Sound Vib.* **405**, 208–233 (2017)
  60. Nugent, S., Posch, H.A.: Liquid drops and surface tension with smoothed particle applied mechanics. *Phys. Rev. E* **62**(4), 4968–4975 (2000)
  61. Obhrai, C., Bullock, G., Wolters, G., Müller, G., Peregrine, H., Bredmose, H., Grine, J.: Violent wave impacts on vertical and inclined walls: large scale model tests. *Coast. Eng.* **2004**, 4075–4086 (2005)
  62. Olshevskiy, A., Dmitrochenko, O., Kim, C.: Three and four noded planar elements using absolute nodal coordinate formulation. *Multibody Syst. Dyn.* **29**(3), 255–269 (2013)
  63. Olshevskiy, A., Dmitrochenko, O., Kim, C.W.: Three-dimensional solid brick element using slopes in the absolute nodal coordinate formulation. *ASME J. Comput. Nonlinear Dyn.* **9**(2), 021001 (2013)
  64. Rafiee, A., Dutykh, D., Dias, F.: Numerical simulation of wave impact on a rigid wall using a two-phase compressible SPH method. *Proc. IUTAM Symp. Part. Methods Fluid Dyn.* **18**, 123–137 (2015)
  65. Randles, P.W., Libersky, L.D.: Smoothed particle hydrodynamics: some recent improvements and applications. *Comput. Methods Appl. Mech. Eng.* **139**, 375–408 (1996)
  66. Randles, P.W., Libersky, L.D.: Private communication (1997)
  67. Ritter, A.: Die Fortpflanzung der Wasserwellen. *Z. Ver. deut. Ing* **36**, 947–954 (1982)
  68. Shabana, A.A.: ANCF reference node for multibody system analysis. *Proc. Inst. Mech. Eng. Part K J. Multi Body Dyn.* **229**(1), 109–112 (2015)
  69. Shabana, A.A.: *Computational Continuum Mechanics*, 3rd edn. Wiley, Chichester (2018)
  70. Shao, J.R., Li, H.Q.: An improved SPH method for modeling liquid sloshing dynamics. *Comput. Struct.* **100–101**, 18–26 (2012)
  71. Shao, J.R., Li, H.Q., Liu, G.R., Liu, M.B.: An improved SPH method for modeling liquid sloshing dynamics. *Comput. Struct.* **100**, 18–26 (2012)
  72. Shi, H., Wang, L., Nicolsen, B., Shabana, A.A.: Integration of geometry and analysis for the study of liquid sloshing in railroad vehicle dynamics. *Proc. Inst. Mech. Eng. Part K J. Multi Body Dyn.* **231**(4), 608–629 (2017)
  73. Tait, M.J.: Modelling and preliminary design of a structure-TLD system. *Eng. Struct.* **30**(10), 2644–2655 (2008)
  74. Teng, B., Zhao, M., He, G.H.: Scaled boundary finite element analysis of the water sloshing in 2D containers. *Int. J. Numer. Methods Fluids* **329**, 4466–4485 (2006)
  75. Vignjevic, R., Campbell, J., Libersky, L.: A treatment of zero energy modes in the smoothed particle hydrodynamics method. *Comput. Methods Appl. Mech. Eng.* **184**(1), 67–85 (2000)
  76. Vishal, M., Sijoy, C.D., Vinayak, M., Shashank, C.: Tensile instability and artificial stresses in impact problems in SPH. *J. Phys. Conf. Ser.* **377**, 012102 (2012)
  77. Wang, L., Octavio, J.R.J., Wei, C., Shabana, A.A.: Low order continuum-based liquid sloshing formulation for vehicle system dynamics. *J. Comput. Nonlinear Dyn.* **10**(2), 021022 (2015)
  78. Wei, C., Wang, L., Shabana, A.A.: A total Lagrangian ANCF liquid sloshing approach for multibody system applications. *ASME J. Comput. Nonlinear Dyn.* **10**(5), 051014 (2015)
  79. Wen, Y., Hicks, D.L., Swegle, J.W.: Stabilising SPH with conservative smoothing. Technical report SAND94-1932, Sandia National Laboratories (1994)
  80. Wu, G.X., Ma, Q.W., Taylor, R.E.: Numerical simulation of sloshing waves in a 3D tank based on a finite element method. *Appl. Ocean Res.* **20**(6), 337–355 (1998)

**Publisher's Note** Springer Nature remains neutral with regard to jurisdictional claims in published maps and institutional affiliations.